

## THE EFFECT OF PHOTOSPHERIC GRANULATION ON THE DETERMINATION OF THE LITHIUM ABUNDANCE IN SOLAR-TYPE STARS

H. UITENBROEK

Harvard-Smithsonian Center for Astrophysics, 60 Garden Street, Cambridge, MA 02138; HUITENBROEK@cfa.harvard.edu

Received 1997 June 20; accepted 1997 December 11

### ABSTRACT

I investigate non-local thermodynamic equilibrium (non-LTE) formation of the 670.6 nm Li I resonance doublet in the presence of convective surface inhomogeneities in solar-type stars. This doublet is widely used for lithium abundance determination in stars. It has been suggested that the presence of hot and cool elements in a stellar atmosphere due to convective heat transport might lead to an underestimate of lithium abundance by as much as a factor of 10 when the equivalent width of the doublet is analyzed in terms of a one-dimensional plane-parallel model atmosphere.

To explore this possibility, I solved the two-dimensional non-LTE radiative transfer equations for a sufficiently large lithium model atom in a hydrodynamic simulation snapshot of the solar granulation. This was done for different values of the lithium abundance ranging from  $A_{\text{Li}} = 0.0$  to 3.3.

In all cases the effects of the inhomogeneities in the atmosphere on lithium line strength are small, never amounting to more than 0.1 dex in the derived abundance. This occurs mainly for three reasons. First, because of the exponential decrease of density with height in the gravitationally stratified stellar atmosphere, radiation escapes mostly vertically with little horizontal exchange. Some lateral transfer does occur at the boundaries between hot and cold elements, but the effect of this exchange on the spatially averaged line strength cancels out. It leads to a smoothing over the surface rather than to a diminishing overall strength of the doublet. Second, the sharp drop in temperature over hot upwelling material, in contrast to the much shallower gradient over the dark intergranular lanes, causes the 670.6 nm doublet to be deeper and narrower in the former and broader in the latter. Consequently, the contrast of equivalent line width between profiles emerging over hot upflows and cold downflows is small. Finally, because of its small abundance the opacity scale in lithium ionizing continua is mostly set by  $\text{H}^-$  bound-free processes. Optical depth unity at the photoionization edges, therefore, follows the contours of electron temperature, moderating contrast in the ionizing radiation field.

*Subject headings:* convection — line: formation — radiative transfer — stars: abundances — stars: late-type — Sun: granulation

### 1. INTRODUCTION

A reliable estimate of the primordial lithium abundance would enable us to constrain, among other things, early universe nucleosynthesis models and the cosmic nucleon-to-photon density ratio  $\eta_{10}$  (see the extensive review by Boesgaard & Steigman 1985). Unfortunately, this primordial abundance is not well known, with more than an order of magnitude difference between current extreme estimates (cf. Spite & Spite 1982). The most important factor in this disparity is the uncertainty in the relation between the amount of lithium in the early universe and that measured at present. Lithium is easily destroyed by  $[^7\text{Li}(p, \alpha)^4\text{He}]$  nuclear reactions at temperatures above  $2.6 \times 10^6$  K. The transport of lithium through mixing in cool star envelopes by convective overshoot, gravitational settling, turbulent diffusion, and rotationally induced meridional circulation consequently causes the surface lithium abundance in these late-type stars to be rapidly reduced over time (e.g., Michaud & Charbonneau 1991). Lithium is, at least partially, replenished through spallation of CNO elements by cosmic rays and in magnetic flares.

Conversely, because lithium is so fragile and its abundance very sensitive to the detailed balance between production and destruction it can be used as tracer of mixing processes in the stellar interior. For instance, the spread in lithium abundance in stars of the same cluster and its dependence on effective temperature and rotation can be

employed to constrain models of stellar structure and evolution (e.g., Michaud & Charbonneau 1991).

In the light of its great value for constraining big bang models and tracing stellar evolution, it is important to eliminate any uncertainties that limit our present-day measurement of lithium abundance from stellar spectra. Lithium has a very low first ionization potential (5.4 eV) making it almost completely ionized even in the coolest of stellar atmospheres. Measuring lines from the first ionization stage is unfortunately not a viable option since these appear in the UV (the resonance lines are at 19.9 nm) where there is little flux in cool stars and where there are many more lines from other elements. The neutral-stage lines fall in the optical and are at least accessible from the ground. Interpretation of the equivalent widths of the neutral-stage lines in terms of abundances may, however, be difficult. It requires accurate knowledge of the degree of ionization as small errors in this balance lead to large uncertainties in the populations of the minority stage, in this case the neutral stage. Even when the ionization equilibrium is well determined, non-LTE effects in the line formation have to be taken into account. For instance, line scattering may enhance the equivalent width of the 670.6 resonance doublet, causing an overestimate of the abundance if the observed profile is interpreted in terms of LTE line formation. Together non-LTE effects in ionization and line transfer can cause the abundance to be over- or underestimated

compared to LTE analysis, depending on effective temperature, metallicity, and surface gravity (Carlsson et al. 1994).

Usually, abundance determinations have relied on one-dimensional static models that represent the stellar atmospheres under consideration in some average sense. The question arises whether analysis of observed spectra in terms of such time- and space-averaged models of stellar atmospheres is valid and provides us with physically realistic values of the atmosphere's mean quantities. Moreover, we may ask what these mean values tell us about the true physics of the plasma. In answering these questions we have to deal with complicated radiative transfer solutions because generalizations of results obtained in static plane-parallel modeling are often not straightforward. Long-range action of radiation through scattering, and interlocking of radiative transitions at widely different wavelengths, may cause the excitation and ionization degrees of a spatially differentiated plasma to be very different from the solution predicted by a combination of homogeneous models with the same average properties. Similarly, the solution at some instant in an evolving plasma may differ considerably from the solution obtained from a static model that gives rise to the same spectrum. Because of the different timescales at which physical processes like ionization, recombination, and excitation occur the history of the plasma has to be taken into account. A striking example is provided by the calculations by Carlsson & Stein (1995), who show that the time-averaged spectrum of a series of hydrodynamic shocks running through an atmosphere without a chromospheric rise in the average temperature can mimic the spectrum of a hydrostatic model with such a chromospheric rise. If we want to extract realistic information from spectroscopic observations in cases like this, especially when these observations are spatially and/or temporally averaged, we may need to solve the complete radiative transfer problem accounting for horizontal radiation exchange and the proper timescales for all relevant transitions. Only when we explicitly perform such detailed calculation can we assess how reliable our diagnostics are and what we exactly measure with them.

It has been shown that magnetically related surface inhomogeneities like stellar spots and plages are unlikely to cause the spread in observed lithium abundances at a given effective temperature (e.g., Stuijk, Bruls, & Rutten 1997). These magnetic phenomena typically have a relatively large spatial scale so that the abundance of a particular star could, in principle, be derived from a filling factor weighted model of its different surface components. The purpose of this paper is to investigate the effects of surface inhomogeneities on a smaller scale (on the order of a photon mean free path length) that could potentially alter the whole character of the line-formation process, making it unrealistic to analyze the spectrum under consideration in terms of a linear combination of separate plane-parallel models.

Kurucz (1995) has suggested that lithium abundances might be severely underestimated (by as much as a factor of 10) in extreme Population II stars because of atmospheric inhomogeneities that are not well accounted for by one-dimensional mixing-length models. In his paper he estimates that radiation from hot upwelling regions depletes lithium in the colder downdrafts where it is less ionized, thus reducing the spatially averaged equivalent width. This conclusion derives from the big contrast in lithium line

strength for hot and cold elements based on estimates from a two-stream mixing-length formulation of the convection. In this paper I use a more physically realistic granulation model based on simulations by Stein & Nordlund (1989) and full two-dimensional radiative transfer to show that, in the particular case of the solar granulation, the mixing-length arguments severely overestimate the actual contrast in line strength.

In this paper I do not attempt to reproduce lithium line formation over a range of different types of stars; very few detailed hydrodynamic calculations of stellar surface convection exist to begin with (see, however, Nordlund & Dravins 1990 for examples). The aim here is rather to understand *how* multidimensional radiation transfer affects lithium line strength in the particular example of the Sun and the solar granulation, so that we can better assess possible sources of errors for other stars due to simplified one-dimensional modeling. To keep the numerical problem tractable in size while solving radiative transfer for many wavelengths and directions and solving the coupled statistical equilibrium equations for many levels simultaneously, I only show results for slabs that vary in depth and in one additional horizontal direction. In general this constraint will lead to an underestimate of the full three-dimensional transfer effects, but, most importantly, it allows us to evaluate the nature of multidimensional transfer mechanisms.

The structure of this paper is as follows. Section 2 describes data that were used for the atomic and atmospheric models and the two-dimensional radiative transfer code that was used to evaluate the variation of lithium line width in the presence of surface inhomogeneities. Section 3 describes lithium line formation in the two-dimensional granulation snapshot. I compare results from these two-dimensional calculations to one- and 1.5-dimensional calculations in § 3.2 and discuss the accuracy of the employed angle discretization in § 3.3. Finally, the paper ends with conclusions in § 4.

## 2. METHOD AND INPUT MODELS

### 2.1. *Input Model Atmosphere*

The lateral transfer effects discussed in this paper were evaluated in a two-dimensional slice of a solar granulation simulation “snapshot” by Stein & Nordlund (1989). The original data cube, which represents a single instant in time in a three-dimensional hydrodynamic simulation, has a  $63 \times 63$  horizontal grid measuring  $6000 \times 6000$  km. It has 47 depth points between  $z = -500$  and 650 km, where  $z = 0$  is defined as the average location of unit optical depth in the vertical direction at a wavelength of 500 nm. Since the radiation field would be completely thermalized in the deepest layers of the original data cube, the transfer calculations were limited to a depth of  $z = -200$  km. To get a better sampling of the vertical scale, the remaining upper part of the cube was interpolated onto a 64 point equidistant vertical grid. Finally, to evaluate the two-dimensional transfer effects, the slice was treated as if it were an infinite slab in the  $y$  direction.

Figure 1 shows the temperature distribution in the simulation snapshot at a height of  $z = -65.1$  km. The position of the employed two-dimensional cut is indicated by the horizontal line at  $y = 2600$  km. It runs through a set of typical granules and intergranular lanes. The topology of

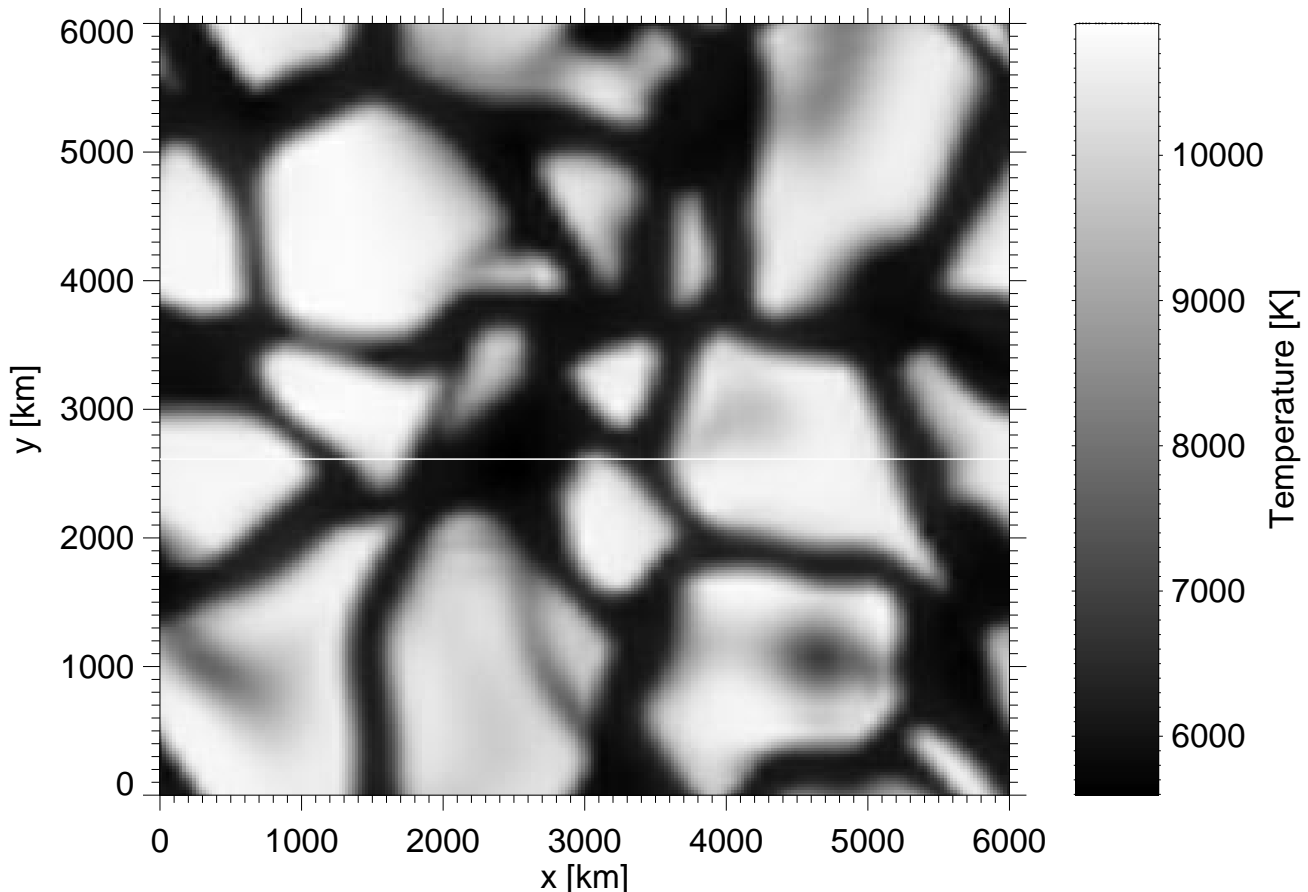


FIG. 1.—Temperature distribution of the Stein & Nordlund (1989) granulation snapshot at an altitude of  $-65.1$  km. The horizontal line indicates the position of the two-dimensional cut used in this paper.

the granular flow is described in detail by Stein & Nordlund (1989). It consists of broad upflowing regions of hot buoyant material and narrow downflow regions where cooled (both due to radiative losses and expansion work) material converges and moves downward. Figure 2 shows the map of the material flow in the two-dimensional cut indicated in Figure 1. The temperature stratification in the cut is depicted as a gray-scale image. At the top of the atmosphere the structure of the simulation is somewhat arbitrary; it has a fiducial layer of 150 km to provide for an open boundary zone to let mass motions go through the actual boundary at 500 km. This scheme results in a constant temperature in the horizontal plane at 650 km. However, conclusions that are drawn for lithium line strength are not affected by this, since line formation occurs at much greater depth.

While the original data cube has macroscopic velocities in all 3 degrees of freedom, the transfer calculations in the two-dimensional slice only account for velocities in the  $x$ - $z$  plane, i.e., the projection of the velocity field onto the plane of the slice.

To evaluate the importance of lateral transfer effects, results of the full two-dimensional transfer solution were compared to so-called 1.5-dimensional calculations. In the latter case the same two-dimensional slab was used, but radiative transfer was solved in each column of the slab separately, independent of neighboring columns. Doppler shifts due to vertical motions were still accounted for in this case, but flow velocities in the  $x$  direction were neglected.

Finally, the results of the two- and 1.5-dimensional calculations were compared to line profiles from a plane-parallel hydrostatic equilibrium model that is representative of the average solar atmosphere. This model XCO was constructed by Avrett and coworkers (Avrett 1995) to match a large number of molecular CO fundamental vibration-rotation lines in the infrared observed with the ATMOS experiment (Farmer & Norton 1989). Such a one-dimensional model has to parameterize small-scale dynamic motions with an assumed microturbulent velocity distribution.

On a depth scale based on the total hydrogen density, the microturbulence assumed for the XCO model is very similar to the distribution in the Vernazza, Avrett, & Loeser (1981) models. This is true even for lithium, which is a light element for which thermal broadening is an important line broadening mechanism. In the granulation-slab modeling no microturbulence was included, assuming that all dynamic motions are resolved by the hydrodynamic simulation. In § 3.2 I will show, however, that model XCO, with its concurrent microturbulence, results in an overestimate of the lithium line strength compared to the spatially averaged line strength from the two-dimensional slab. To investigate whether this overestimate was due to the assumed microturbulence in model XCO, I also computed line strengths in a model that had zero microturbulence but was similar to XCO otherwise. This model is referred to as XCO\_vt0.

Computations of lithium line formation were done with different lithium abundances ranging from  $A_{\text{Li}} = 0.0$  to 3.3

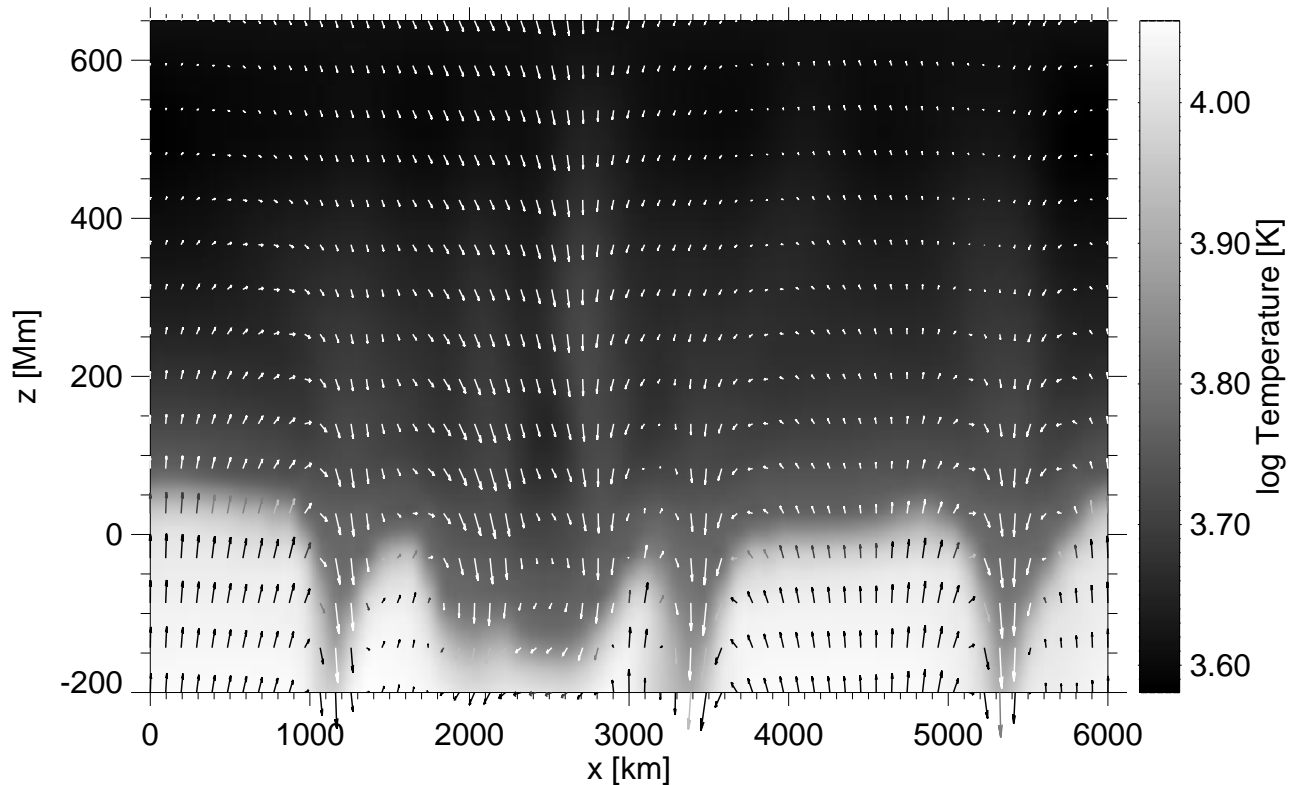


FIG. 2.—Arrows indicate flow velocity in the two-dimensional slice through the Stein & Nordlund (1989) granulation simulation snapshot. The temperature stratification in the slice is given by the gray-scale image.

on the standard scale where  $A_{\text{Li}} \equiv \log(n_{\text{Li}}/n_{\text{H}}) + 12$ . The highest value of 3.3 corresponds to the abundance found in young objects like T tauri stars that supposedly have not undergone any depletion, and to solar system meteorites. It is assumed to be the initial abundance in the young Sun, before it depleted its lithium to the current value of  $A_{\text{Li}} = 1.1$ . While assuming different lithium abundances, it was assumed that abundances of other metals remain unchanged so that the pattern of the convection is the same for all considered amounts of lithium.

## 2.2. Background Opacities and Molecular Formation

All major background opacity sources were included in the transfer calculations. These include Thomson scattering between photons and free electrons; Rayleigh scattering from neutral hydrogen, helium atoms, and  $\text{H}_2$  molecules;  $\text{H}^-$ ,  $\text{H}_2^+$ , and neutral hydrogen bound-free and free-free processes; and opacity due to bound-free transitions of metals, i.e., elements other than hydrogen and lithium. The effect of line blanketing due to metallic UV lines on the radiative ionization rates was not taken into account. Including the additional line opacity would not be difficult. However, prescribing the concurrent source functions in a general (i.e., not requiring LTE) yet realistic way is still an unsolved problem in stellar atmosphere modeling (Avrett 1996). The conclusions drawn in this paper will not be affected by this omission, since they depend on the relative behavior of the cold and hot elements in the granulation simulation.

The formation of molecules was accounted for in the background opacity calculations, and the population

numbers of elements that are chemically bound were reduced accordingly. Although the binding energy of the LiH molecule (2.43 eV) is less by a factor of 2 than the lithium first ionization potential, it is worthwhile to investigate how much lithium gets bound into LiH. Especially in cool stars this might be a substantial fraction. Figure 3 shows the ratio of lithium atoms bound in the molecule LiH to the amount of neutral lithium for the highest lithium abundance ( $A_{\text{Li}} = 3.3$ ) considered. LiH quickly dissociates at temperatures above  $T = 9 \times 10^3$  K, even at the higher densities near the bottom of the model. In this particular slice never much more than 0.1% of the neutral lithium fraction gets absorbed into the hydride. It can be shown as follows that this holds true also for the lower lithium abundances considered here. The equation for chemical equilibrium for LiH is

$$n_{\text{LiH}} = n_{\text{Li},1} n_{\text{H},1} Q(T), \quad (1)$$

where  $n_{\text{LiH}}$  is the molecular number density,  $n_{\text{Li},1}$  and  $n_{\text{H},1}$  are the number densities of the ground states of lithium and hydrogen, respectively, and  $Q$  is the equilibrium constant. Since  $n_{\text{H},1}$  is essentially independent of the amount of lithium-hydride that forms, the ratio  $n_{\text{LiH}}/n_{\text{H},1}$  does not change with  $A_{\text{Li}}$ . The equilibrium constant was calculated from the tables provided by Sauval & Tatum (1984).

Note the plumes of slightly lower LiH concentration above the dark intergranular lanes (at  $x = 1200, 3400$  and  $5500$  km) indicative of higher local temperatures. Over the hot granules the LiH concentration is higher (between heights  $z = 200$ – $400$  km) corresponding to slightly lower temperatures. This reversal of granular contrast is observed in the cores of moderately strong spectral lines and in the

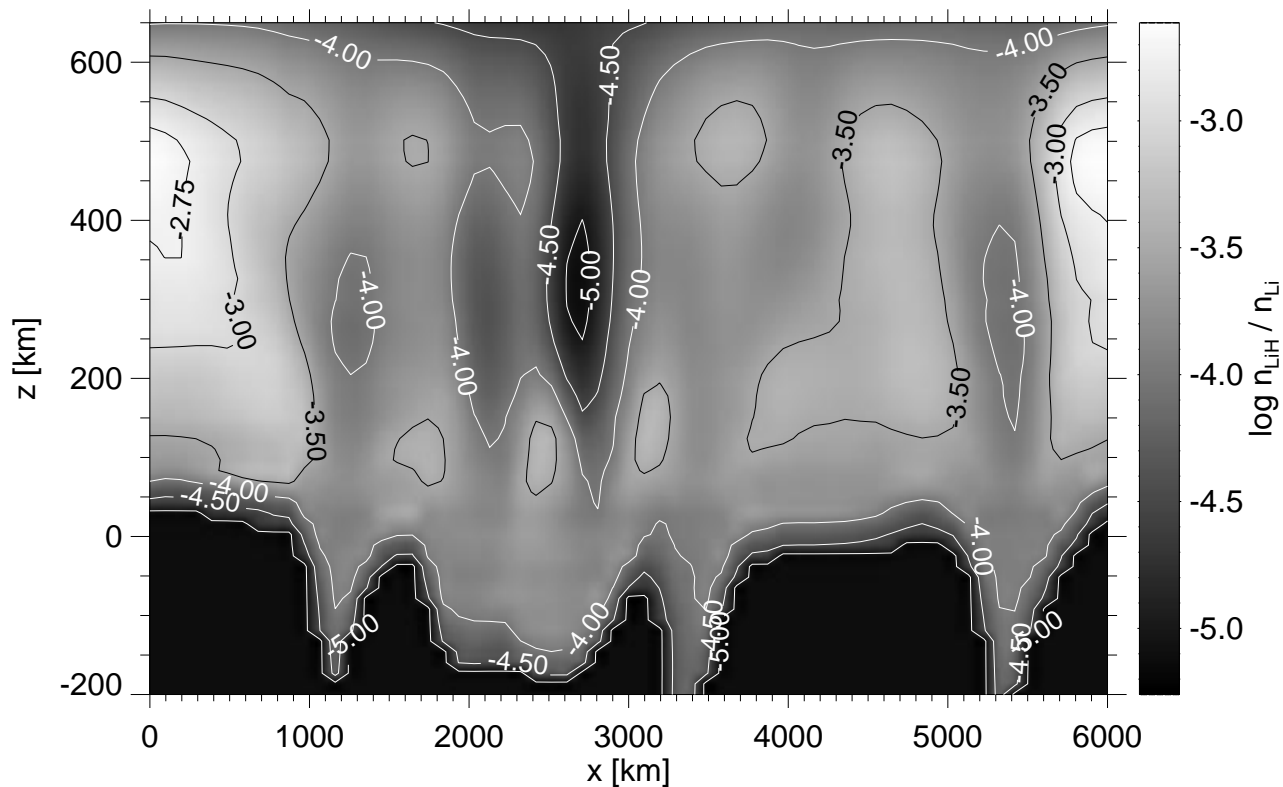


FIG. 3.—Gray-scale plot depicting the ratio of the number of lithium atoms bound in LiH relative to the number of neutral lithium atoms for a total lithium abundance  $A_{\text{Li}} = 3.3$ .

wings of strong lines like the Ca II H and K lines (Evans & Catalano 1972). It stems from the dynamics of the convection in the gravitationally stratified atmosphere. As the upflowing hot gas enters low-density layers it cools radiatively and has to expand rapidly horizontally so that it cools even more. When the horizontal flow is retarded over the intergranular lanes, the gas is compressed and consequently heated again. During its horizontal motion the gas is also radiatively heated (see Nordlund 1984).

No transfer computations were attempted with lower overall metallicity, since the whole structure of the granulation would be very different and the model would be internally inconsistent. Calculations of stellar granulation have been done for different effective temperatures and surface gravity (e.g., Nordlund & Dravins 1990). However, no detailed hydrodynamic calculations exist with low metallicities, so we can only guess how the granular pattern and with it the effect of lateral transfer on the lithium equivalent width will be affected. A lower metallicity will in general reduce the opacities even in regions where the  $\text{H}^-$  is the dominant opacity source because the number of negative hydrogen ions depends on the electron density. This in turn would make the temperature gradient less shallow with depth resulting, in general, in lower velocity convective flows.

### 2.3. Radiative Transfer

Two new radiative transfer codes named RHF1D and RHSC2D were used to compute non-LTE emergent line profiles of the Li I 670.6 resonance doublet in one- and two-dimensional geometry. These codes share the same implementation of the Multilevel Accelerated Lambda Iteration (MALI) scheme developed by Rybicki & Hummer

(1991, 1992). They will be described in more detail in a separate paper. The one-dimensional version RHF1D uses the familiar Feautrier second-order difference scheme (Feautrier 1964; Auer 1967; Auer 1976) for the formal solution of the transfer equation with a given source function. The two-dimensional code RHSC2D uses the so-called short characteristics method (Kunasz & Auer 1988) with periodic horizontal boundary conditions as described by Auer, Fabiani Bendicho, & Trijillo Bueno (1994). In both RHF1D and RHSC2D overlapping lines and continua are treated consistently with full preconditioning of the rate equations as described by Rybicki & Hummer (1992). Ng's (1974) acceleration technique is employed in both codes to improve the rate of convergence where necessary.

The angle sets of Carlson (1963) were used in the two-dimensional code to perform the integration of intensity over solid angle. Most calculations presented below were done with his angle set A4 with three rays per octant. The influence of angle discretization on the disk-center equivalent width of the 670.6 nm doublet is discussed in § 3.3. In one-dimensional modeling all calculations were done with a three-point Gauss-Legendre quadrature for the azimuth angle.

### 2.4. Model Atom

The lithium model atom used for the spectral synthesis in this paper is illustrated with its Grotrian diagram in Figure 4. It is complete only to principal quantum number  $n = 3$ , with nine levels and 11 lines. The fine structure is kept explicitly since RHF1D and RHSC2D can handle overlapping bound-bound and bound-free transitions; there is no need for combining levels into terms. The model is less complete than the one employed by Carlsson et al. (1994)

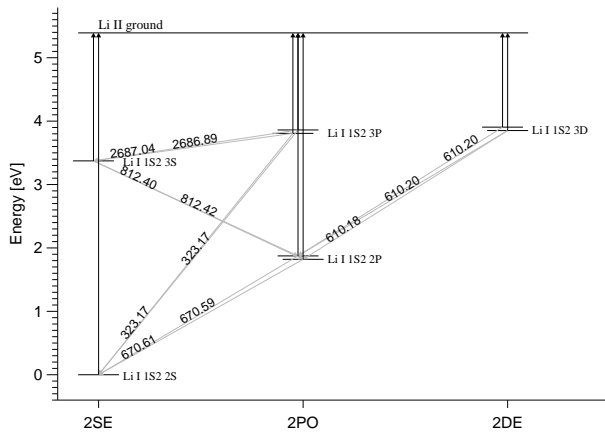


FIG. 4.—Term diagram of the lithium model atom

mainly to reduce the computational effort in the two-dimensional transfer calculations. The omission of the higher levels will slightly increase the ionization fraction of lithium as it makes the recombination flow (through collisions and IR lines between the higher excitation levels) from the majority singly ionized stage more difficult (see Carlsson et al. 1994; Bruls, Rutten, & Shchukina 1992 for a similar effect in the formation of K I and Na I lines). The equivalent width found in the spatially averaged XCO model in the present calculations is in close agreement with the value of 16 pm for a one-dimensional radiative equilibrium solar model quoted by (Stuik et al. 1997, see their Fig. 5). These authors use a lithium model very similar to the one employed by Carlsson et al. (1994). Therefore, the smaller atom should be adequate for our purpose here.

Level energies and oscillator strengths were taken from the compilation by Kurucz (his CD ROM 18).<sup>1</sup> Photoionization cross sections are from the opacity project (Peach, Saraph, & Seaton 1988).

Bound-bound electron collision strengths for optically allowed transitions were calculated with Seaton's (Seaton 1962) impact approximation while Van Regemorter's (1962) approximation with an oscillator strength of  $f = 0.1$  was used for optically forbidden transitions. Collisional strengths for bound-free transitions were computed with Seaton's formula as given by Allen (1976).

Radiative broadening as calculated from the level lifetimes was included, as well as collisional broadening by neutral hydrogen and helium (Van der Waals damping). The latter was calculated with Unsöld's (Unsöld 1955) classical formula without any additional multiplicative factor. Such a factor is not needed here as it is usually intended to compensate for line broadening due to small-scale velocities and opacity broadening due to thermal inhomogeneities, both of which are inherent to the granulation snapshots employed here (see also Nordlund 1984, and Bruls & Rutten 1992). No Stark broadening by electrons and ions was taken into account.

### 3. LITHIUM LINE FORMATION IN GRANULATION SLABS

Lithium line formation in one-dimensional plane-parallel atmospheres and the non-LTE mechanisms that affect its

line strength have been extensively discussed by Carlsson et al. (1994). Here I will briefly repeat their conclusions in order to facilitate the discussion of two-dimensional transfer effects later in this section. The five main mechanisms that describe lithium non-LTE behavior are resonance line scattering, photon suction, ultraviolet overionization, infrared overrecombination, and bound-bound pumping. For relatively high lithium abundances, resonance line scattering propagates photon line losses to optical depths much larger than one. The result is line strengthening because the increased lower level population shifts line formation outward to lower temperatures. The combined photon losses from the resonance lines and lines higher up in the term diagram may result in even larger overpopulation of the lithium ground state through the enhanced recombination through higher excitation levels they cause. This process was called "photon suction" by Bruls et al. (1992). In solar-type atmospheres this overpopulation is counteracted by ultraviolet overionization that occurs because the mean intensity  $J_\nu$  decreases more gradually with height than the Planck function  $B_\nu$  when temperature gradients are steep enough as is the case in the deep photosphere. Compared to LTE the ionization balance will shift toward higher ionization when  $J_\nu - B_\nu > 0$  over the most important bound-free edges. For lithium the most important photoionization threshold is the one from the first excited level (which is the upper level of the 670.6 nm doublet) at 349.7 nm where  $J_\nu - B_\nu$  is largest in the solar photosphere. The effect of overionization on the 670.6 nm doublet is a shift to lower height of formation and a weakening of the line.

The remaining two processes, infrared overrecombination and bound-bound pumping, are less important for lithium line formation and don't play a role in the two-dimensional transfer effects discussed here.

Figure 5 shows the vertically emergent spectrum of the 670.6 nm resonance doublet from the two-dimensional granulation simulation slab. There is strong variation, not only in line-profile shape, but also in line and continuum intensity. Dark intergranular lanes like the ones at  $x = 1200$ , 3400, and 5500 km are easily recognized by their large redshift connected to the converging downflow of cooled matter (compare Fig. 2), and their lower continuum intensity. Bright granules are characterized by higher continuum intensity and narrower profiles. Two relative-intensity line profiles characteristic of a "hot" granule center (*solid curve*) and "cool" intergranular lane (*dashed curve*) are displayed in Figure 6. Remarkably, once scaled to the adjacent continuum intensity at the proper spatial location, the profiles have almost the same equivalent width, the granular profile being somewhat deeper and the intergranular lane profile relatively broader. The main cause for this is the much steeper temperature gradient over the hot granule, which tends to increase contrast between line and continuum. It compensates the equivalent width for the decrease in line opacity due to enhanced overionization over the hot granules. The drop in temperature in the lanes is much more gradual due to the compression heating of horizontally converging material (see § 2.2).

Figures 7 and 8 show the departure coefficients  $\beta_1$  and  $\beta_2$  of the  $2s$  ground level, and the sum of the two  $2p$  first excited states. The coefficient  $\beta_i$  is defined as the value of the population number  $n_i$  of level  $i$  with respect to its LTE value. The general pattern of the two departure coefficients

<sup>1</sup> See also the URL <http://cfa-www.harvard.edu/amp/data/stats/kurucz.html>.

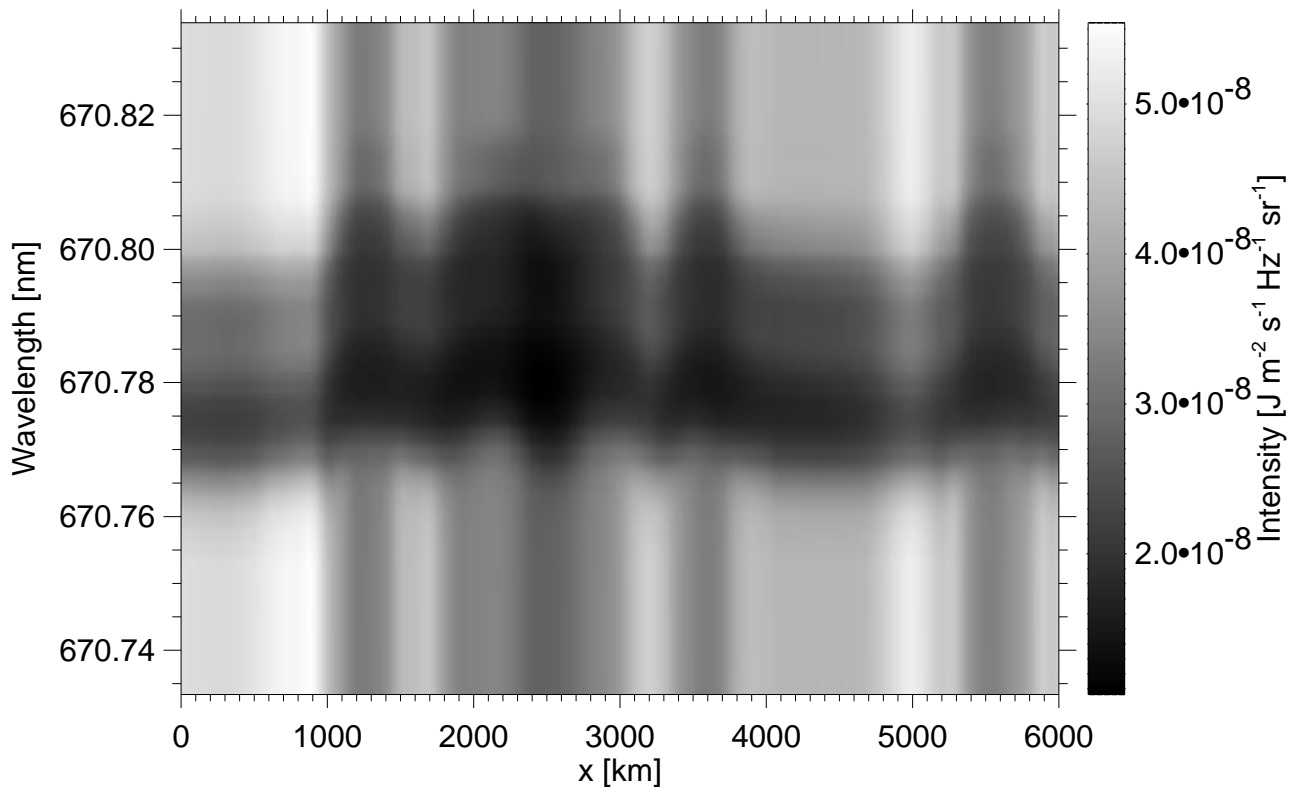


FIG. 5.—Calculated emergent intensity profile for the Li I resonance doublet at disk center from the two-dimensional cut indicated in Fig. 1

with height in the atmosphere is very similar to the one described by Carlsson et al. (1994, their Fig. 4) for one-dimensional modeling in a plane-parallel radiative equilibrium model. For the ground-level departure coefficient the main difference with the radiative equilibrium modeling is the absence of the pronounced rise in  $\beta_1$  over the hot granules. In radiative equilibrium modeling this rise occurs at line center optical depth  $\tau = 0.1$  (corresponding to  $z = 200\text{--}300$  km) as a result of the combined Li I line photon losses (i.e., photon suction). In the two-dimensional

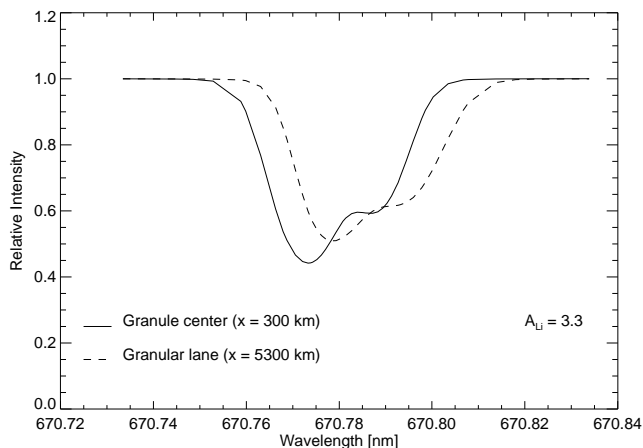


FIG. 6.—Calculated relative-intensity line profiles for the Li I resonance doublet at disk center for two locations in the two-dimensional slab. These profiles are representative of a granule (solid curve) and intergranular lane (dashed curve). Each profile is normalized to the adjacent continuum at its proper spatial location.

slab the steep temperature gradient over the granules caused by the strong expansion and radiative cooling of the hot upwelling matter results in higher overionization and a reduction of line opacity with respect to background opacity. In this case resonance scattering becomes less important as photons are more likely to be destroyed by a continuum process. Over the cool intergranular lanes with their more shallow temperature gradient the rise is present (and even more pronounced than in the one-dimensional radiative equilibrium model) because there is less overionization.

Similarly, the departure coefficient  $\beta_2$  of the second level behaves very much like the one in the radiative equilibrium case, where it decreases monotonically outward as a result of resonance scattering. There are three locations where the pattern is markedly different. First, consider the small areas with  $\beta_2 \approx 1$  at  $x = 1100$  and  $5300$  km and  $z = 0$  km. These are indicative of two-dimensional transfer in the doublet itself. The radiation from the hot walls of the dark lanes is able to locally populate the  $2p$  state over the low excitation values in the dark lanes. The long upwardly extending bright finger corresponds to a high-temperature, high electron density, and low hydrogen density region in the simulation snapshot. It is most likely a dark lane that is about to form. In this finger there is additional electron collisional excitation to counteract the drop off of the departure coefficient due to photon losses in the resonance line. The same is true, although to a lesser extent, for the small fingers extending above the already existing intergranular lanes.

The line source function  $S^l$ , which is effectively proportional to  $\beta_2/\beta_1$ , apart from stimulated emission, is shown in Figure 9 as the ratio  $S^l/B_\nu$ . Optical depth unity in the doublet measured vertically from the top of the atmo-

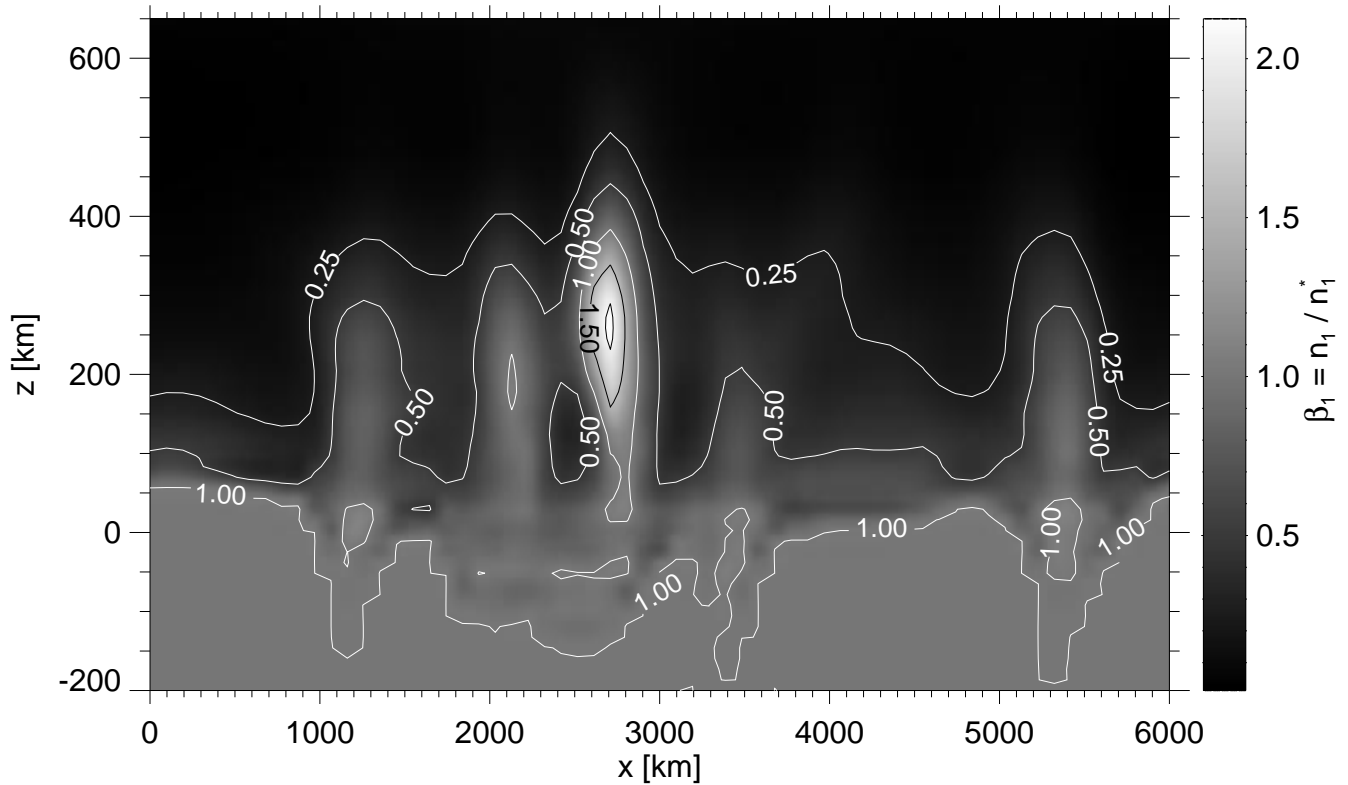


FIG. 7.—Departure coefficient  $\beta_1 = n_1/n_1^*$  of the 2s level

sphere is marked by the thick line. In the Eddington-Barbier relation the vertically emergent intensity at wavelength  $\nu$  is given by  $I_\nu \approx S(\tau_\nu = 1)$ . Above the hot granule between  $x = 5600$  and  $1000$  km (the simulation has

periodic boundary conditions) the radiation field in the doublet itself raises the source function at heights  $z = 400$ – $500$  km, but this is at very low optical depth and will not affect the emergent line intensity.

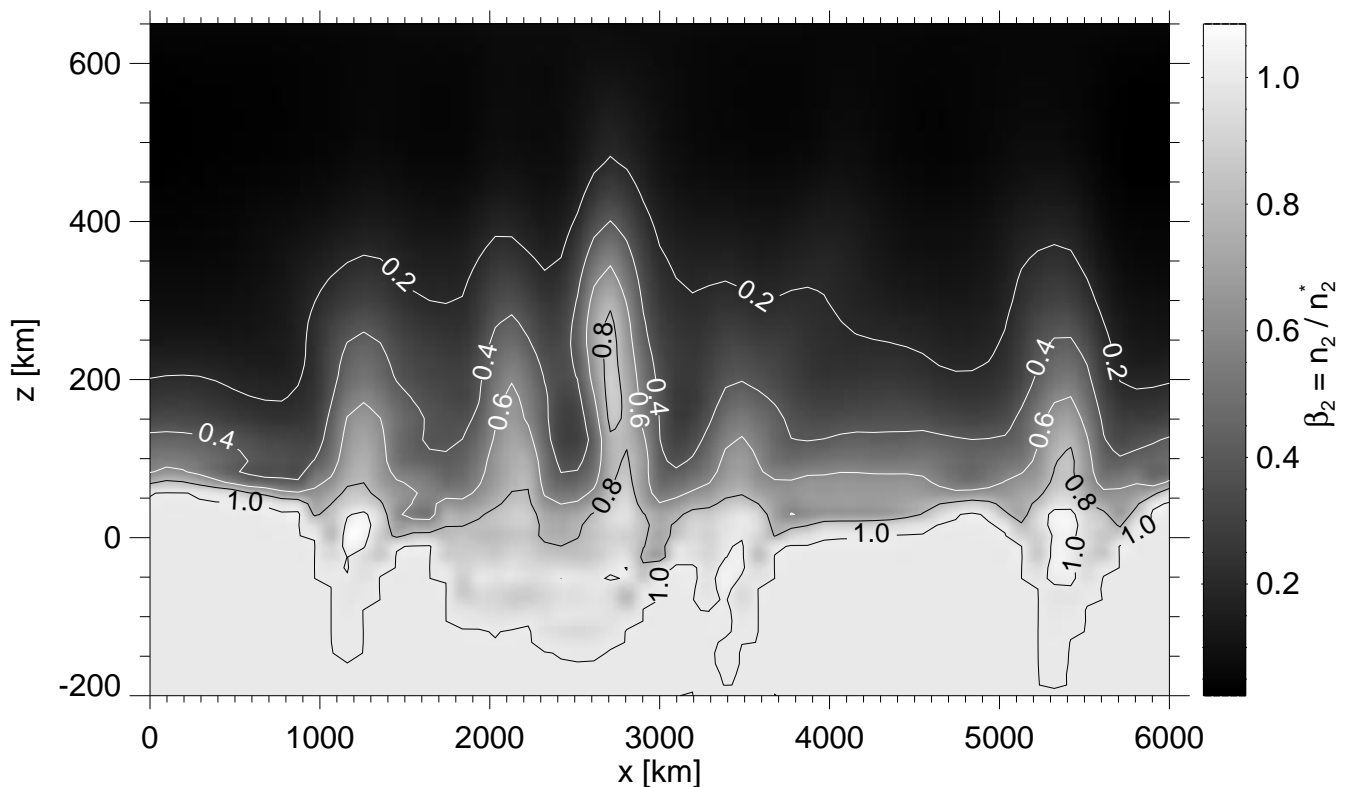


FIG. 8.—Departure coefficient  $\beta_2 = n_2/n_2^*$  of the combined 2p levels

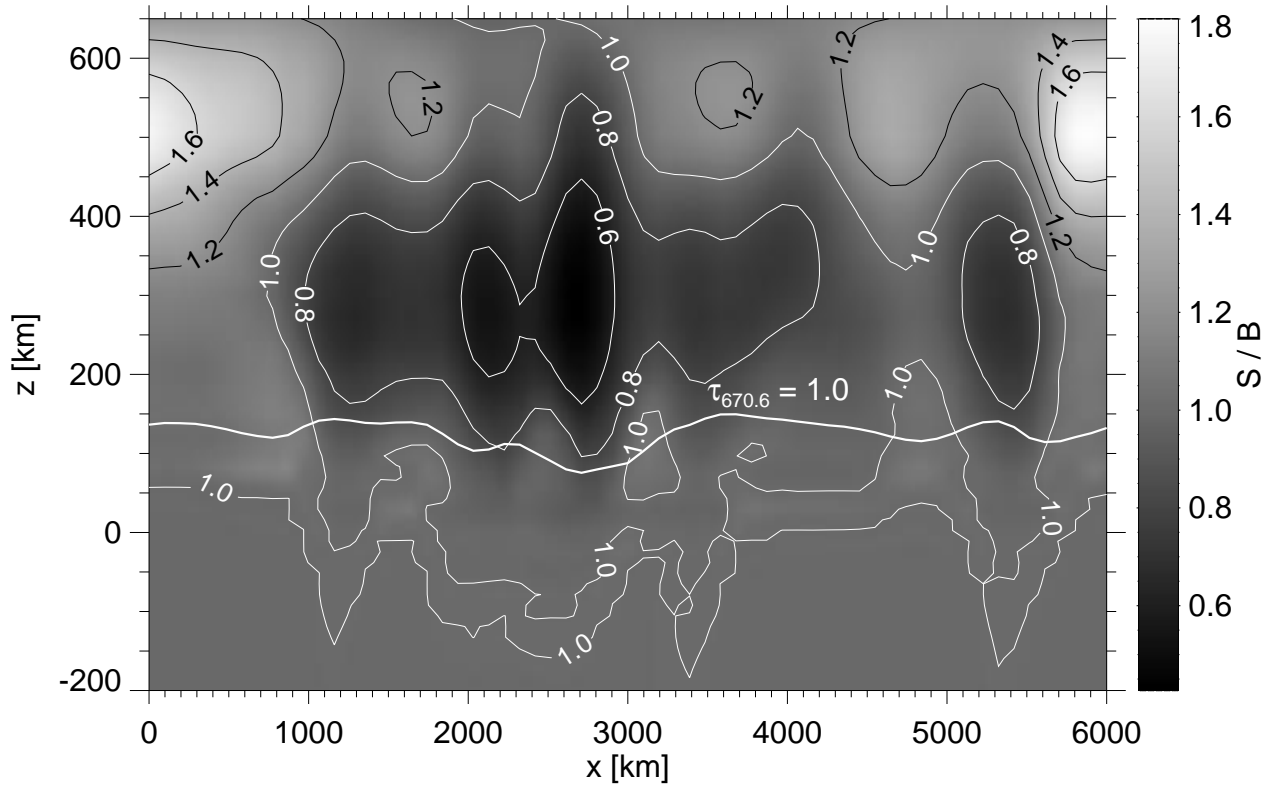


FIG. 9.—Ratio of the source function  $S^l$  at a wavelength close to the center of the 670.6 nm resonance doublet to the Planck function at that wavelength. The curve indicates the location of total (i.e., line plus background) optical depth unity in the vertical direction.

### 3.1. Difference between 1.5- and Two-dimensional Results

To differentiate between the effects of lateral transfer on one side and variations in the emergent line strength due to horizontal variations in the vertical stratification through the grid on the other side, calculations were done in the so-called 1.5-dimensional approximation. In this case radiative transfer was solved separately in each of the 63 columns of the two-dimensional granulation slab as if they were semi-infinite plane-parallel atmospheres. Figure 10 shows the ratio of the neutral fractions,  $f_{2D}$  and  $f_{1.5D}$ , respectively, for both cases, where  $f = n_{Li}^{neutral}/n_{Li}^{total}$ . The arrows in Figure 10 show the direction and magnitude of the radiative flux  $F_{349.7}$  at the wavelength of the  $2p$  bound-free edge, where

$$F_v = \int I(n, \nu) n d\Omega. \quad (2)$$

The two curves mark the optical depth unity from the two-dimensional calculation, as measured vertically from the top of the atmosphere, in the doublet (*solid curve*) and at the  $2p$  edge (*dashed curve*). The bright and dark streaks in the upper half of the graph signify under- and over-ionization, respectively, of the 1.5-dimensional case with respect to the full two-dimensional transfer case.

When the ionizing radiation field decouples from the local electron temperature at about  $\tau_{349.7} = 1$  two-dimensional transfer allows radiation from localized hot elements (e.g., at  $x = 1600, 3100,$  and  $4900$  km) to spill into neighboring regions. This reduces the ionization over the hot elements with respect to the 1.5-dimensional case, where

such lateral transfer cannot take place, causing the bright streaks, and increases the relative ionization over the neighboring colder elements, giving rise to the darker streaks in Figure 10. The nature of the lateral transfer is clearly visible in the direction of the flux vectors. The lateral extent and the amplitude of the dark and bright streaks are both comparable, so that the total ionization (integrated over  $x$ ) at all heights is very similar in the 1.5- and two-dimensional cases.

Lateral transfer in the ionizing radiation field only takes place at and directly above the  $\tau_{349.7} = 1$  line and over horizontal distances that are of the order of a few vertical scale heights (typically 200–300 km). Below this curve the ionizing radiation field is thermalized and there is no difference between 1.5- and two-dimensional transfer. A few scale heights above optical depth unity the radiation flow is almost entirely vertical, and no further lateral transfer takes place. This is because the slab is much more uniform in its upper layers and because scattering that becomes increasingly important with height tends to make the radiation field more isotropic. Over broad features like the granular centers between  $x = 5900$  and  $700$  km the 1.5-dimensional approximation is accurate, and the ratio  $f_{2D}/f_{1.5D}$  is very close to one.

This behavior with lateral transfer effective over only short horizontal distances stems from the exponential density stratification of the atmosphere in a gravitational field. It can be understood with the following simple line of reasoning (cf. Jones 1986). Let the opacity be density dependent and given by  $\chi(z) = \chi^{top} \exp[-(z^{top} - z)/H]$ , where  $H$  is the opacity scale height and  $z$  the geometric height in the atmosphere. Then at great depths (several scale heights

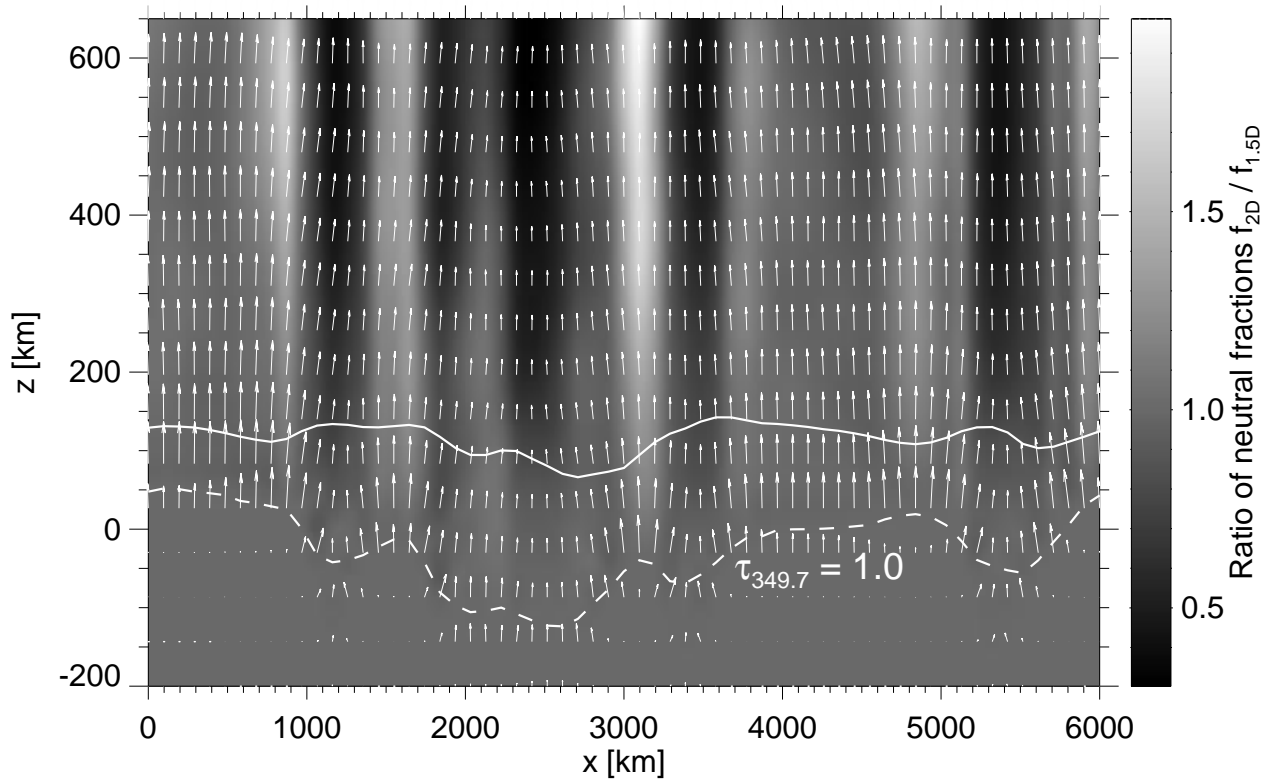


FIG. 10.—Ratio of ionization fractions for the 1.5- and two-dimensional calculation. The arrows indicate the direction of the radiative flux at the wavelength of the bound-free continuum edge from the first excited level at 349.7 nm. The two curves mark the location of optical depth unity in the vertical direction at the wavelength of the 670.6 nm doublet (solid line) and bound-free edge at 349.7 nm (dashed curve).

below the surface) the vertical optical depth is given by

$$\tau(z) = \int_{z_{\text{top}}}^z \chi(z') dz' \approx H\chi(z). \quad (3)$$

The horizontal optical extent of a structure of size  $L$  is  $L\chi(z)$ . Now horizontal transport can only become important if the lateral photon escape probability is equal to or larger than the probability of vertical escape. This condition is satisfied when  $L < \alpha H$  with  $\alpha$  of order unity.

We now come to an important issue that in part explains the low contrast between ionizing radiation emerging over hot elements like granules on the one hand and cold elements like intergranular lanes on the other hand. The opacity of the most important bound-free edge at 349.7 nm is almost completely determined by the  $\text{H}^-$  bound-free process (in the absence of UV line blanketing). This opacity is very temperature sensitive. When the temperature rises, more electrons become available and the  $\text{H}^-$  opacity rises, pushing intensity formation outward to lower temperatures. Consequently, optical depth unity, which for the  $2p$  edge is marked by the dashed curve in Figure 10, tends to follow the contours of the electron temperature. The ionizing radiation field thus decouples from the local conditions at very similar temperatures for all  $x$  values, even though the electron temperature at a specific *geometrical* height may vary substantially (this mechanism is also mentioned by Avrett (1990), see his Fig. 12). In addition, between the height at which the ionizing radiation field at 349.7 nm decouples and the height at which the resonance doublet decouples (i.e., the area between the dashed and solid curves), differences between 1.5-dimensional and two-dimensional have only

partially developed and have only limited influence on the emergent line strength. For lower lithium abundances this is even more true, since the location of the dashed  $\tau = 1$  curve is independent of atmospheric lithium content and the solid curve will go to lower altitudes. Similarly, adding UV line haze to the background opacity will bring the formation of line and ionization edge closer together, and this will consequently tend to reduce the effect of lateral radiation transfer on the strength of the 670.6 nm doublet.

### 3.2. Equivalent Widths

Stellar abundances are determined from the equivalent width of the disk-integrated flux profile by relating the measured equivalent width to a theoretical curve of growth that is constructed from an assumed model of the star under consideration. Figure 11 shows the position-dependent equivalent width of the flux profile of the  $\text{Li I } 670.6$  nm doublet for four different lithium abundances  $A_{\text{Li}} = 0.0, 1.1, 2.0,$  and  $3.3$  for the two-dimensional (solid curves) and 1.5-dimensional (dashed curves) cases. All values are scaled to the value of the equivalent width of the spatially averaged model XCO with zero microturbulence (indicated by the dotted line in each graph) at the same abundance. The absolute values of the spatially averaged equivalent widths in all cases are listed in Table 1. Remarkably, the spatially averaged model XCO without microturbulence almost exactly reproduces the spatially averaged equivalent widths of the resonance doublet in the case of the two-dimensional transfer calculation, while the 1.5-dimensional calculation gives slightly higher values. The last line in Table 1 lists the equivalent width of the standard XCO model that gives approx-

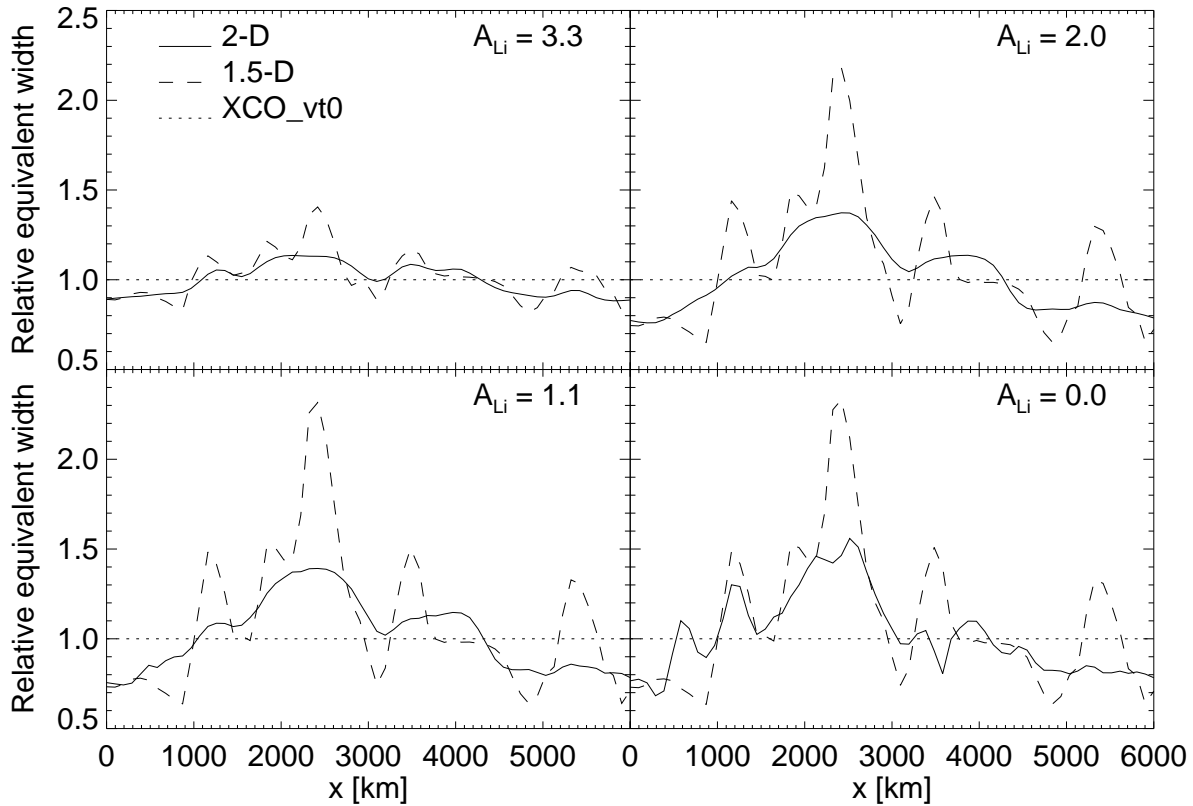


FIG. 11.—Equivalent widths of the emergent flux profiles as a function of position in the slab for the two-dimensional (*solid curves*) and 1.5-dimensional (*dashed curves*) case. For each of the four abundances  $A_{\text{Li}}$  the curves are scaled to the equivalent width from model XCO\_vt0 (indicated by the dotted line in each panel) at that abundance. The spatially averaged true equivalent widths are given in Table 1.

ciably higher line strengths. This means that either the spatially averaged model XCO overestimates the unresolved dynamic motions and assumes too much microturbulence, or, alternatively (and more likely), the dynamic simulation does not resolve all small-scale eddies and the assumption of no microturbulence in the two-dimensional calculation underestimates the real-life line broadening that the spatially averaged model is constructed to match.

The lowest values in the equivalent width of the 1.5-dimensional calculation correspond to intergranular lanes where the gradual decrease in temperature with height produces shallow line profiles. The highest values in equivalent width occur roughly between  $x = 1800$  and  $2800$  km (see also Fig. 5). In this area the density between  $z = -150$  and  $100$  km drops relatively slowly with height. Presumably this is an area in which a downflow is forming and where material is being compressed. As a result of the density stratification there is considerable vertical distance between  $\tau = 1$  in the  $349.7$  nm continuum edge and the line-

formation height (compare the dashed and solid lines in Fig. 10). Therefore, while the continuum comes from a relatively shallow temperature gradient resulting in low continuum intensities (see Fig. 5) and low overionization (see Fig. 7), the line itself forms in a region where the gradient is relatively steep, resulting in a deep and broad profile. The same is true, to lesser extent, for the region between  $x = 5200$  and  $5700$  km.

The detailed differences between the two-dimensional and 1.5-dimensional calculations are due to lateral transfer effects as described in §§ 3 and 3.1. Lateral transfer makes the ionizing radiation field more homogeneous on horizontal spatial scales of a few opacity scale heights (see Fig. 10), and this smooths the equivalent width over the surface but almost preserves the spatially integrated line strength. The 1.5-dimensional case gives slightly higher values for all considered abundances due to the nonlinearity of the Planck function at the wavelength of the  $349.7$  nm edge; even when surface areas of hot and cold regions affected by lateral

TABLE 1  
SPATIALLY AVERAGED EQUIVALENT WIDTHS FOR THE Li I 670.6 nm DOUBLET  
FOR THE DIFFERENT RADIATIVE TRANSFER MODELS

MODEL	$A_{\text{Li}}$ (pm)			
	0.0	1.1	2.0	3.3
Two-dimensional .....	$1.65 \times 10^{-2}$	$2.06 \times 10^{-1}$	$1.56 \times 10^{+0}$	$1.64 \times 10^{+1}$
1.5-dimensional .....	$1.76 \times 10^{-2}$	$2.20 \times 10^{-1}$	$1.65 \times 10^{+0}$	$1.67 \times 10^{+1}$
XCO_vt0 .....	$1.62 \times 10^{-2}$	$2.02 \times 10^{-1}$	$1.54 \times 10^{+0}$	$1.64 \times 10^{+1}$
XCO .....	$2.02 \times 10^{-2}$	$2.52 \times 10^{-1}$	$1.90 \times 10^{+0}$	$1.85 \times 10^{+1}$

exchange are equal, the excess radiation produced by hot elements will more than make up for the deficit in the colder elements when lateral transfer is effective.

With decreasing abundance the spatial variation between the two-dimensional and 1.5-dimensional solution in Figure 11 first increases (for  $A_{\text{Li}} = 2.0$  and 1.1) and then decreases again. When the lithium abundance decreases the line-formation height goes down, while the formation height of the ionizing radiation field is unaffected (as it is determined by  $\text{H}^-$  bound-free opacity). The line thus forms in more and more inhomogeneous parts of the atmosphere, resulting in the large spatial variations in the 1.5-dimensional solution while lateral transfer in the line itself and in the ionizing continuum radiation washes the differences out in the two-dimensional case. We can expect this picture to change only slightly if we would consider the full three-dimensional transfer problem instead of the two-dimensional approximation employed here (see the Appendix). At the lowest lithium abundance the line forms so close to the formation height of the ionizing continuum, however, lateral transfer in the latter can no longer horizontally smooth the neutral lithium population between the two formation heights, leading to a closer agreement between 1.5-dimensional and two-dimensional solutions.

I do not show a graph with abundance corrections that should be applied when analyzing abundances with a one-dimensional average model. In the first place the sample here is the smallest possible, being only one star. Second, uncertainties that are due to the assumed microturbulence are larger than the difference between the 1.5-dimensional and two-dimensional results. Even compared to the XCO model that includes microturbulence, the inhomogeneous models show abundance corrections that amount to less

than 0.1 dex over the whole abundance range considered here.

### 3.3. Accuracy of Angle Integration in the Presence of Inhomogeneities

The radiative rates that determine population numbers in a non-LTE radiative transfer solution have to be evaluated from the intensities in a discrete set of wavelengths and angles. This discretization limits the accuracy with which the solution is known. In the case of an inhomogeneous atmosphere this is especially true for the angle discretization, since a ray in a specific direction samples only a very limited part of the grid and not the whole spatial grid, as is the case for a one-dimensional plane-parallel atmosphere. Whenever a ray in a specific direction dissects a small-scale inhomogeneity, the intensity in that direction will be biased to the properties of the inhomogeneity, and with it the mean intensity of all locations along the ray. If, in addition, there are macroscopic velocities present, a proper wavelength sampling of lines cores is also important.

To estimate the magnitude of possible errors due to angle-discretization, a calculation was done in the two-dimensional granulation snapshot with a very fine angular mesh of 10 rays per octant (Carlson's 1963 set A8). To calculate disk-center intensities in both cases, the radiative transfer equation was first solved with both angle sets (neither of which includes a ray in the vertical direction). Then the calculated population numbers, background opacities, and mean intensities were used to solve for the emergent intensity in each case in the vertical direction. Figure 12 shows the relative difference of disk-center intensity around the 670.6 nm doublet for the sets A4 and A8. In the nearby continuum (the gray areas at the top and near the bottom of

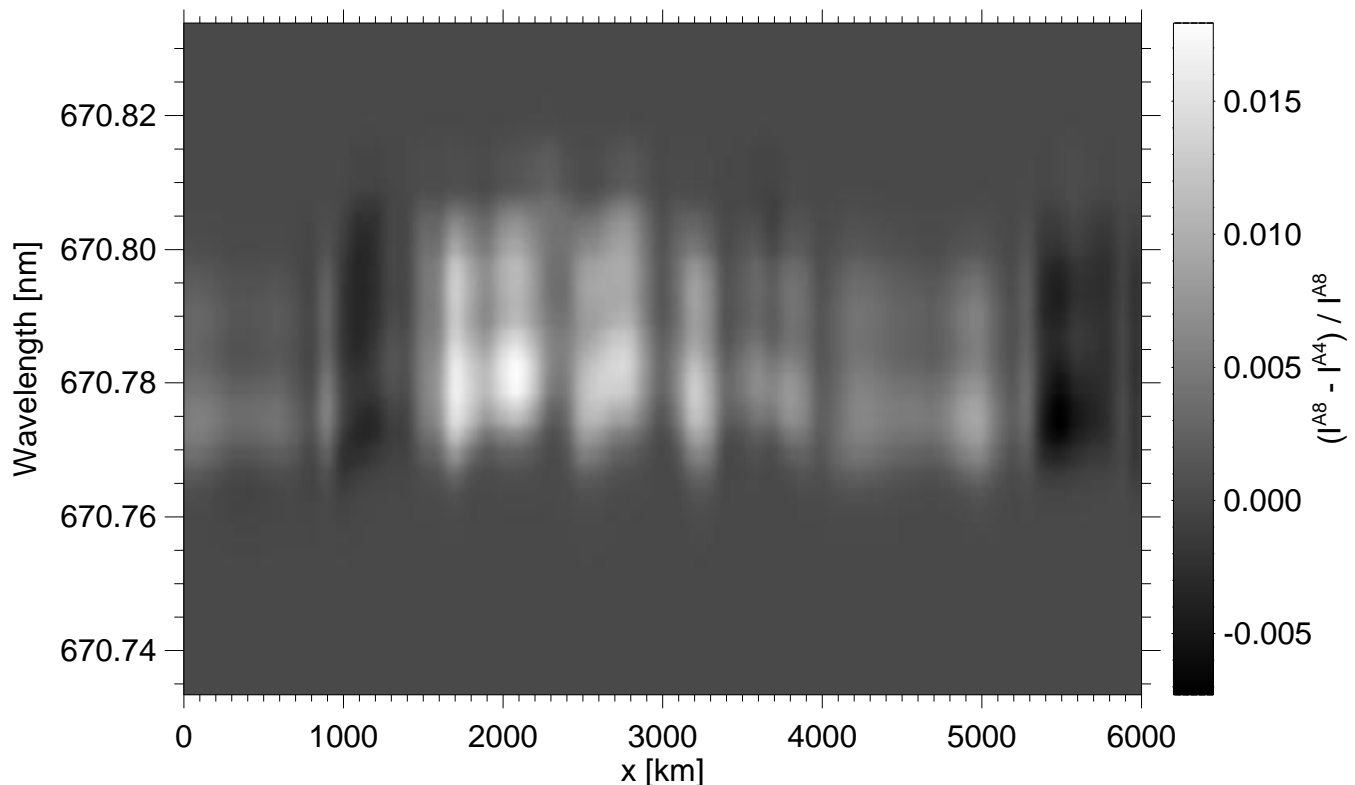


FIG. 12.—Relative difference between disk-center intensities of the Li I resonance doublet computed with two different angle quadratures: Carlson's (1963) sets A4 and A8 with three and 10 rays per octant, respectively.

the panel) there is no distinction in intensity between the two sets. In the doublet itself there are small differences of up to 1.5% in intensity. Mostly, the line is slightly brighter with the fine angular grid A8. The reason for this is the steep gradient in temperature just above the hot granular elements. With a coarse angular grid this sharp drop-off in the vertical direction is not well sampled; the radiation field is underestimated because shallow angles that sample more hot material are underrepresented (the same would hold in a one-dimensional calculation). This undersampling mainly affects the ionizing radiation field because of the nonlinearity of the Planck function in the UV. Therefore, lithium will be slightly more ionized and the line slightly weaker with the more complete angular grid A8. In fact, the ratio of the population numbers  $n_2/n_1$  is very similar in both cases (not shown here) with relative differences below 4% over the whole grid, while both  $n_1$  and  $n_2$  differ by up to 17% between the two angle discretizations. Note that the largest discrepancies occur only higher up in the atmosphere and are inconsequential for the line intensities. Transfer in the line is less affected by the strong temperature gradient because the line is still thermalized there. The continuum radiation, on the other hand, decouples right at the location of the strong gradients, which are there to begin with exactly because radiative losses set in at those heights.

Over the darkest intergranular lanes (at  $x = 1100$  and  $5500$  km) the situation is reversed and the doublet is darker in the case of the A8 angular grid by about 0.5%. This is a multidimensional transfer effect. In the case of the lower resolution angular grid the angular mean intensity is overestimated in those locations over the dark lanes where two rays emanating from the two opposite bright side walls of the lanes meet. If this happens in a zone where the doublet forms it will be slightly brighter with the lower resolution angular grid, which is exactly the case at  $x = 1100$  and  $5500$  km.

#### 4. CONCLUSIONS

Detailed two-dimensional non-LTE radiative transfer calculations of lithium line formation in an inhomogeneous model of the solar atmosphere show that inhomogeneities have little effect on the accuracy with which lithium abundances can be derived from the strength of the Li I 670.6 nm resonance doublet. This is true for all lithium abundances considered here ranging from  $A_{\text{Li}} = 0.0$  to 3.3. Measured abundances never differ more than 0.1 dex when the spatially averaged equivalent width from an inhomogeneous model like the granulation slab employed here are interpreted in terms of a curve of growth constructed from a one-dimensional plane-parallel model. This is in stark contrast with estimates derived from mixing-length formulation of the convection, which predict that abundance determinations may be underestimated by as much as a factor of 10 (Kurucz 1995). With the analysis presented here, I find there are three main reasons that lead to the conclusion that the lithium line strength has a weak sensitivity to atmospheric inhomogeneities. One of these reasons is related to multidimensional radiative transfer, while the other two stem from the nature of the hydrodynamical simulation and the temperature-density stratification it creates, which is markedly different from the one predicted by mixing-length arguments. The mixing-length formulation of the convection does not allow the temperature contrast inversion, with higher temperatures over cold intergranular lanes and

lower temperatures over hot granules, in the stable layer into which the granulation penetrates. This inverted contrast leads to deep *relative* intensity profiles (from which the equivalent width is determined) over the hot granules, and to shallow profiles over the intergranular lanes. A second important factor is the fact that the opacity at the main lithium ionization edge at 349.7 nm is determined by  $\text{H}^-$  opacity. This causes the radiation formation height to follow more or less the contours of temperature resulting in low horizontal contrast in the ionizing radiation field. Together these two effects cause the Li I 670.6 nm doublet to actually appear weakest over the dark intergranular lanes where it is predicted to be much stronger (than over the hot upwelling granules) in the mixing-length formulation (see Table 3 in Kurucz 1995). Clearly, even judging from the small sample of the granulation simulation that is represented by the slab employed in this paper, there is no general pattern by which all the granular forms and shapes can be classified, indicating that the mixing-length formulation indeed lacks some important details of the convective flows.

The most important multidimensional radiative transfer effect is the lateral transfer in the ionizing radiation field that takes place between regions of adjacent hot and cold matter. This transfer takes place over only a few scale heights horizontally and spatially smooths the ionizing radiation field. It enhances the total ionization only slightly, judging from the slightly higher spatially averaged equivalent widths in Table 1 for the 1.5-dimensional calculation compared to the two-dimensional results. The rather small sensitivity of the shape of the emergent line profiles to the employed angle discretization discussed in § 3.3 also seems to point to a rather minor influence of lateral transfer on lithium line strength.

The conclusions drawn above remain true even if we had considered three-dimensional transfer instead of limiting ourselves to two dimensions; the main reason for the weak sensitivity of the Li I line strength to atmospheric inhomogeneities is the different vertical stratification found over the hot and cold convection elements that compensates for the difference in overionization.

Whether the conclusions presented in this paper will be different for stars of different type and, more specifically different metallicity, is hard to assess in the absence of detailed hydrodynamical convection simulations in those cases. This would be especially interesting with respect to the discrepancy that exists for estimates of the primordial lithium abundance from low- and high-metallicity stars. The convection in the outer layers of a star is essentially driven by the radiative losses at the stellar surface. Thus, the spatial scales at the surface are more or less determined by the opacity scale height. On the other hand, the dynamical spatial scales depend on the density scale height, which is of the same order of magnitude as the opacity scale height (in the case of opacity dominated by  $\text{H}^-$  the density scale height is about twice the opacity scale height). For instance, a typical granular size is determined by the continuity of mass flux when the hot upflow turns into a sideways motion over the height range in which strong radiative losses start to occur

$$\rho\pi R^2 v_z = \rho 2\pi R H v_r, \quad (4)$$

where  $R$  is the typical radius of an upflow region,  $H$  a density scale height, and  $v_z$  and  $v_r$  the velocities of upflow

and sideways motion, respectively. We find  $R = H v_r / v_z$ . So unless  $v_z$  and  $v_r$  are very different, typical sizes are of the order of a scale height. As discussed in § 3.1 multidimensional transfer effects occur over horizontal spatial scales of an opacity scale height, and we may expect very similar behavior of the multidimensional transfer solution, even if

the absolute scales of convection change considerably with metallicity.

This work was supported by NASA grants NAG 5-3106 and NAGW-2545.

## APPENDIX

### THE VALIDITY OF THE TWO-DIMENSIONAL TRANSFER SOLUTION

This appendix shows, with a simple example, that the two-dimensional approximation of the radiative transfer solution employed in this paper should be reasonably accurate. It compares the mean intensity on the axis of a vertical three-dimensional cylindrical structure due to an outside radiation field to the radiation field on the midplane of its two-dimensional approximation, a vertical slab with thickness twice the cylinder radius. We assume an isotropic radiation field  $I_0$  outside the structure and in the interior only account for absorption. The material inside the structure has constant opacity, and the radial optical thickness in the cylinder is  $\tau$ . The angle-averaged mean intensity  $J$  is defined by:

$$J = \frac{1}{4\pi} \int I(\Omega) d\Omega . \quad (5)$$

If we choose the  $z$ -axis along the axis of the cylinder and use the common notation  $\mu = \cos(\theta)$ , where  $\theta$  is the angle with the  $z$ -axis, then the equation for the radiation field on the cylinder axis is

$$J = I_0 \int_0^1 \exp(-\tau/\mu) d\mu , \quad (6)$$

where  $I_0 \exp(-\tau/\mu)$  is the intensity in direction  $\mu$  due to the outside radiation field. Using the transformation  $\alpha = 1/\mu$ , we can rewrite this as

$$J = I_0 \int_1^\infty \alpha^2 \exp(-\tau\alpha) d\alpha = I_0 E_2(\tau) , \quad (7)$$

where  $E_2$  is the second exponential integral.

Now consider the radiation field on the midplane of the slab in the two-dimensional approximation to this problem. The walls of the structure are now two planes parallel to the  $z$ - $y$  plane. The optical thickness along the  $x$ -axis from the midplane to either wall is  $\tau$ . Let  $\tau$  be the angle with the  $x$ -axis. Then the equation for the mean intensity can be rewritten in *exactly* the same way as equation (7) with obviously the same result. Thus, the mean radiation field on the midplane of the two-dimensional approximation in this simple example is exactly the same as that on the axis of the original cylinder. In realistic situations, when opacities vary with height, there will, of course, be differences between the radiation field in the full three-dimensional solution and in the two-dimensional approximation, but this example indicates that these are not likely to be large.

## REFERENCES

- Allen, C. W. 1976, *Astrophysical Quantities* (London: Athlone)
- Auer, L. 1967, *ApJ*, 150, L53
- Auer, L., Fabiani Bendicho, P., & Trijillo Bueno, J. 1994, *A&A*, 292, 599
- Auer, L. H. 1976, *J. Quant. Spectrosc. Radiat. Transfer*, 16, 931
- Avrett, E. H. 1990, in *IAU Symp. 138, Solar Photosphere: Structure, Convection, and Magnetic Fields*, ed. J.-O. Stenflo (Dordrecht: Kluwer), 3
- . 1995, in *Infrared Tools for Solar Astrophysics: What's Next*, ed. J. R. Kuhn & M. J. Penn (Singapore: World Scientific), 303
- . 1996, in *IAU Symp. 176, Stellar Surface Structure*, ed. K. G. Strassmeier & J. L. Linsky (Dordrecht: Kluwer), 503
- Boesgaard, A. M., & Steigman, G. 1985, *ARA&A*, 23, 319
- Bruls, J. H. M. J., & Rutten, R. J. 1992, *A&A*, 265, 257
- Bruls, J. H. M. J., Rutten, R. J., & Shchukina, N. G. 1992, *A&A*, 265, 237
- Carlson, B. G. 1963, in *Methods in Computational Physics*, ed. B. Alder, S. Fernbach, & M. Rotenberg (New York: Academic), 1, 1
- Carlsson, M., Rutten, R. J., Bruls, J. H. M. J., & Shchukina, N. G. 1994, *A&A*, 288, 860
- Carlsson, M., & Stein, R. F. 1995, *ApJ*, 440, L29
- Evans, J. W., & Catalano, C. P. 1972, *Sol. Phys.*, 27, 299
- Farmer, C. B., & Norton, R. H. 1989, *A High-Resolution Atlas of the Infrared Spectrum of the Sun and the Earth Atmosphere from Space*, NASA Ref. Pub. 1224, Vol. 1
- Feautrier, P. 1964, *Comput. Rend.*, 258, 3189
- Jones, H. P. 1986, in *Small-Scale Magnetic Flux Concentrations in the Solar Photosphere*, ed. W. Deinzer, M. Knölker, & H. Voigt (Göttingen: Abhandl. Akad. Wiss.), 127
- Kunasz, P. B., & Auer, L. H. 1988, *J. Quant. Spectrosc. Radiat. Transfer*, 39, 67
- Kurucz, R. L. 1995, *ApJ*, 452, 102
- Michaud, G., & Charbonneau, P. 1991, *Space Sci. Rev.*, 57, 1
- Ng, K. C. 1974, *J. Chem. Phys.*, 61, 2680
- Nordlund, Å. 1984, in *Small-Scale Dynamical Processes in Quiet Stellar Atmospheres*, ed. S. L. Keil (Sunspot: NSO), 181
- Nordlund, Å., & Dravins, D. 1990, *A&A*, 228, 155
- Peach, G., Saraph, H. E., & Seaton, M. J. 1988, *J. Phys. B*, 21, 3669
- Rybicki, G. B., & Hummer, D. G. 1991, *A&A*, 245, 171
- . 1992, *A&A*, 262, 209
- Sauval, A. J., & Tatum, J. B. 1984, *ApJS*, 56, 193
- Seaton, M. J. 1962, *Proc. Phys. Soc. London*, 79, 1105
- Spite, F., & Spite, M. 1982, *A&A*, 115, 357
- Stein, R. F., & Nordlund, Å. 1989, *ApJ*, 342, L95
- Stuik, R., Bruls, J. H. M. J., & Rutten, R. J. 1997, *A&A*, 322, 911
- Unsöld, A. 1955, *Physik der Sternatmosphären* (2d ed.; Berlin: Springer)
- Van Regemorter, H. 1962, *ApJ*, 136, 906
- Vernazza, J. E., Avrett, E. H., & Loeser, R. 1981, *ApJS*, 45, 635